

NASA/CR-2001-211232
ICASE Report No. 2001-31



Three-dimensional Flow in Cavity at Yaw

Alex Povitsky
ICASE, Hampton, Virginia

ICASE
NASA Langley Research Center
Hampton, Virginia

Operated by Universities Space Research Association



National Aeronautics and
Space Administration

Langley Research Center
Hampton, Virginia 23681-2199

Prepared for Langley Research Center
under Contract NAS1-97046

October 2001

THREE-DIMENSIONAL FLOW IN CAVITY AT YAW

ALEX POVITSKY*

Abstract. This study is motivated by three-dimensional flows about protrusions and cavities with an arbitrary angle between the external flow and rigid elements. The novel type of a “building block” cavity flow is proposed where the cavity lid moves along its diagonal (Case A). The proposed case is taken as a typical representative of essentially three-dimensional highly separated vortical flows having simple single-block rectangular geometry of computational domain. Computational results are compared to the previous studies where the lid moves parallel to the cavity side walls (Case B). These 3-D lid-driven cavity flows are studied by numerical modeling using second-order upwind schemes for convective terms. The volume and plane integrals of primary and transversal momentum are introduced to compare cases in a quantitative way. For the laminar flow in the cubic cavity, the integral momentum of the secondary flow (which is perpendicular to the lid direction) is about an order of magnitude larger than that in Case B. In Case A, the number of secondary vortices substantially depends on the Re number. The secondary vortices in the central part of the cavity in Case A distinguishes it from Case B, where only corner secondary vortices appear. For a rectangular 3-D 3 : 1 : 1 cavity the integral momentum of the secondary flow in Case A is an order of magnitude larger than that in the benchmark cases. The flowfield in Case A includes a curvilinear separation line and non-symmetrical vortices which are discussed in the paper. The estimated Görtler number is approximately 4.5 times larger in Case A than that in Case B for the same Re number. This indicates that in Case A the flow becomes unsteady for smaller Re numbers than in Case B. For developed turbulent flow in the cubic cavity, the yaw effect on amplification of secondary flow is as strong as that for the laminar flow despite the more complex vortical flow pattern in benchmark case B.

Key words. three-dimensional cavity flow, flow at yaw, separated flow, incompressible flow, vortical flow, laminar and turbulent flow

Subject classification. Fluid Mechanics

1. Introduction. The lid-driven cavity flow mimics many aeronautical, environmental, and industrial flows [10, 12, 2]. The study [2] includes a detailed description of cavity-type flows in chemical engineering. Authors [10] characterize the cavity flow problem as an ideal vehicle for studying complex environmental flows in a simple geometry. Recent aeronautical motivation comes from the problem of airframe noise. The deployment of the trailing-edge flaps, the leading-edge slats, and the undercarriage become one of the important sources of aircraft noise at landing phase of flight [6, 20, 9]. Enclosures of quite different scales are formed by wheel wells, brace boxes, and pin cavities in various joints linking different gear components. Wheels and axles comprise a series of short cylinders of different aspect ratios and inclinations relative to the flow direction. Therefore, noise suppression associated with wheel-well cavity and inter-wheel gap calls for detailed investigation of 3-D cavity-type flows. The experimental studies [7, 8], motivated by landing gear noise, demonstrate that acoustic pressures of high intensity may be obtained in cavities yawed to certain angles even if the flow does not show any significant oscillations for cavities normal or parallel to the mean flow direction.

*Senior Staff Scientist, ICASE, NASA Langley Research Center, Hampton, VA 23681-2199 (e-mail: aeralpo@icase.edu). This research was supported by the National Aeronautics and Space Administration under NASA Contract No. NAS1-97046 while the author was in residence at ICASE, NASA Langley Research Center, Hampton, VA 23681-2199.

In previous studies, the cavity flow was driven by a lid which moves in the direction parallel to the cavity side walls. This flow was studied numerically [12, 10, 5], experimentally [13, 2], and has become a benchmark case for developers of numerical methods [3, 22, 19], to name a few in each category. The flow is almost 2-D at low Re numbers, transforms to the 3-D flow with secondary vortices in the spanwise plane at moderate Re numbers, and bifurcates from a stationary flow to a periodical flow at a critical Re number. The flow loses its symmetry and starts to induce longitudinal vortices which, in turn, lead to turbulence [5, 10]. The critical Re number depends upon depth-to-width and length-to-width aspect ratios. This problem is characterized by quite simple geometry and boundary conditions and complicated vortical structure of the flow.

In real life, a flow is likely to be non-parallel to the cavity walls. The cavity may be of non-unity aspect ratio and the flow character may range from steady laminar to fully developed turbulent. To study broader cases than that described above and keep the simple geometrical framework, we consider the lid that moves along its diagonal (denoted as Case A here, see Fig. 1a). The flow impinges in the spatial angle formed by the front and a side wall that leads to formation of the system of vortices caused by flow separation. In spite of the lower level of the primary flow velocity (in the direction of the moving lid), the numerous secondary vortices (in the perpendicular direction) appears to be substantially stronger than those in Case B.

We investigate this flow numerically for Re numbers corresponding to existence of steady laminar solution. The flowfield and integrals of primary and secondary momentum are compared to those in the benchmark Case B. The location of vortices and their dependence on the Re number appears to be quite distinctive from that in Case B. Next, we simulate the flow in the 1 : 1 : 3 depth-to-width-to-length rectangular 3-D cavity at yaw. The yaw-related enhancing of secondary flow leads to even more complex pattern of secondary vortices than that for the cubic cavity. Finally, we consider the developed turbulent cavity flow and obtain the amplification of the secondary flow for cavity at yaw. Again, the yaw-related amplification of the secondary flow leads to more than one order of magnitude increase of transversal momentum in comparison to Case B.

The study is composed as follows. In Section 2, the problem arrangement, the mathematical model, boundary conditions, used numerical method, and validation of the computer code are described. In Section 3, the features of primary flow are discussed. In Section 4, the vortical flow patterns of secondary flow are presented and compared to those in Case B. In Section 5, the study has been expanded to fully developed turbulent flows and to rectangular (non-cubic) cavities. In Section 6, conclusions and future work are summarized.

2. Mathematical model, numerical method, and code validation. The governing equations are the three-dimensional steady Navier-Stokes equations. The boundary conditions describe no-slipping and non-penetrating requirements at the steady walls and at the moving lid (see Figs. 1a, b).

In Fig. 1, the considered computational volume is a 3-D cube with its edge equal to unity. In Fig. 1a (Case A), the lid moves in its own plane in the direction of its diagonal. The primary flow (in the direction of moving lid) will be presented in the main diagonal plane CP and planes $CP2$ and $CP3$, which are parallel to CP . These sections are 2-D rectangles with aspect ratios $\sqrt{2} : 1$, $1 : 1$, and $0.5 : 1$, respectively.

To calculate the Görtler number, the velocity profile will be plotted along lines ML and RL in the CP plane (see Section 5). The former line crosses the boundary layer between the primary vortex and the cavity wall while the latter line corresponds to the radial direction of the primary vortex. The flow perpendicular to the direction of the moving lid is denoted as the secondary flow and will be shown at plane PP to study flow motion from the cavity bottom. The vortex flow pattern will be shown in the mid-plane MP , where $y = 0.5$ (see Section 4).

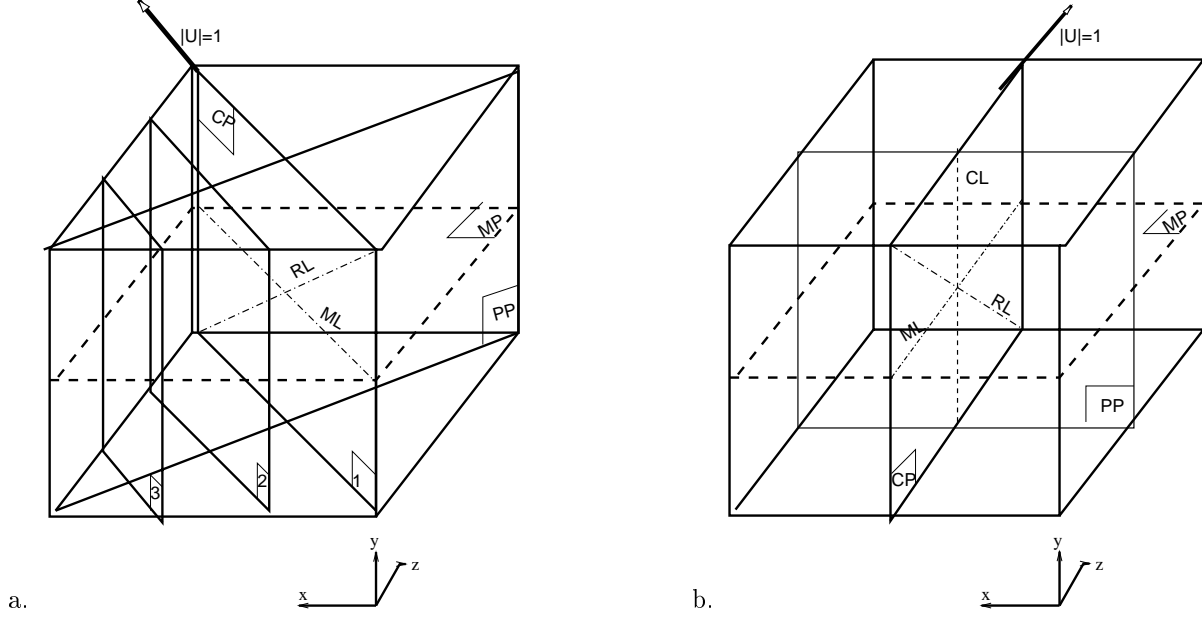


FIG. 1. Cavity flow: a) Case A: The lid moves along its diagonal; b) Case B: The lid moves parallel to a side wall.

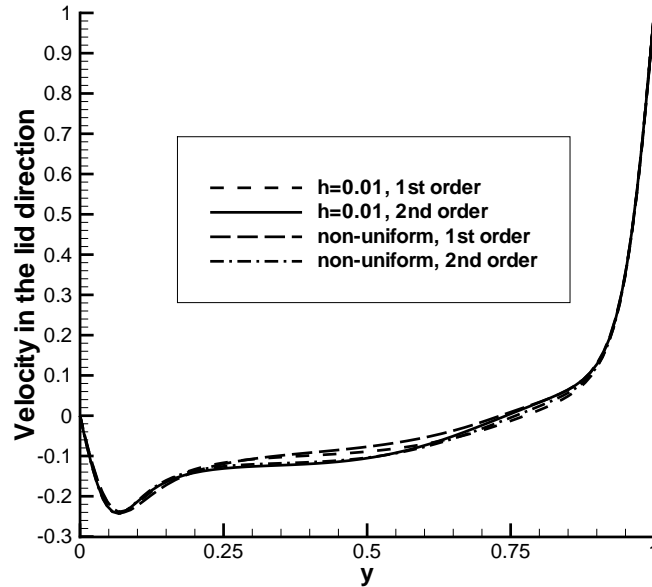
For Case B (Fig. 1b), the velocity vector field in planes CP , PP , and MP will be shown for comparison of computational results to Case A. These planes have the same orientation with regard to the direction of the moving lid as those in Case A. For code validation purposes, the velocity profiles along the vertical centerline CL for various numerical grids and discretizations of governing equations will be discussed later in this Section.

The governing equations are discretized on uniform and non-uniform three-dimensional grids using second-order upwind schemes for convective terms [11], second-order central differences for diffusion terms, and second-order approximation for pressure. The FLUENT software [1] with the second-order upwind discretizations [4] is used in this study. FLUENT uses SIMPLE-type [17] algorithm SIMPLER [21] to resolve velocity and pressure coupling and algebraic multigrid (AMG) to solve the Poisson pressure correction equation.

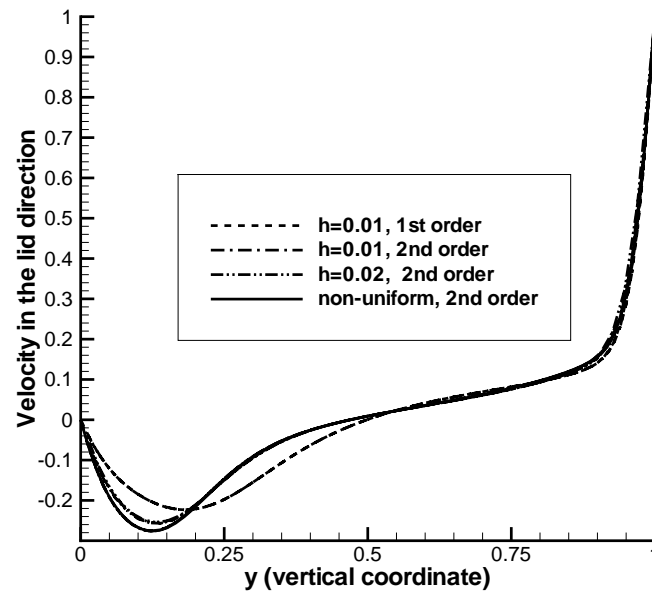
To validate the code, uniform and non-uniform numerical grids are exploited. The uniform numerical grids with $h = 0.02$ ($51 \times 51 \times 51$) and $h = 0.01$ ($101 \times 101 \times 101$) are used. The non-uniform grid is stretched near rigid boundaries. The smallest grid size $h = 0.007$, the ratio of grid sizes for two neighboring nodes is 1.05. The non-uniform part of the grid includes 20 rows at each side; therefore, the maximum (the 20th) mesh size is equal to 0.177 and the non-uniform part occupies $2 \times 23.14\%$ of the edge. The central part is covered with the uniform grid ($h = 0.02$). The total number of grid nodes is 68^3 , which is 3.2 times less than for the 101^3 uniform numerical grid.

For Case A, the profile of the primary velocity $(U + W)/\sqrt{2}$ along the line CL is plotted in Fig. 2a. The results of the second-order computations are closed for the $h = 0.01$ uniform grid and for the non-uniform grid, described above. Results of the first-order computations on the same grids are slightly different while $0.3 \leq y \leq 0.6$.

For Case B, the computational results are compared to the pseudo-spectral [14] and the second-order [3] numerical solutions. In Fig. 2b, the computed primary velocity W along the centerline is presented for $Re = 1000$. For the second-order upwind approximation, the obtained velocity profiles are closed to each



a.



b.

FIG. 2. Validation of the computer code: profile of primary velocity at the cavity centerline CL : a) Case A; b) Case B.

other on both uniform grids. The profiles obtained using the 101^3 uniform grid and the non-uniform grid coincide with the benchmark results [3, 14]. On the contrary, the first-order computations on the 101^3 uniform grid show discrepancy with the benchmark profile. Computational results presented in the next sections were obtained in the non-uniform grid described above.

3. Primary flow. Computed velocity vector field in the plane CP for Case A is presented in Fig. 3. This section represents a rectangle with the aspect ratio $\sqrt{2} : 1$. The primary vortex is shifted towards the

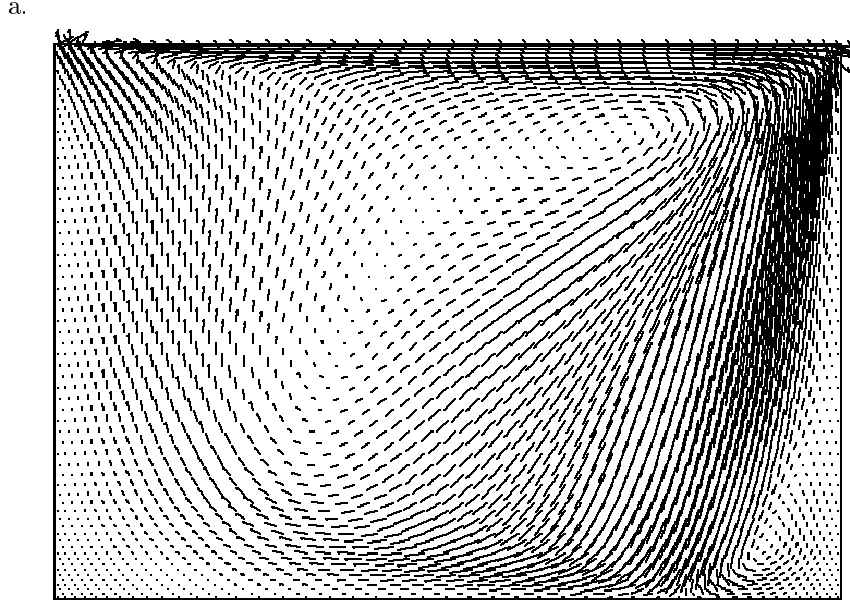


FIG. 3. Case A: primary flow in the $CP1$ plane, $Re = 700$

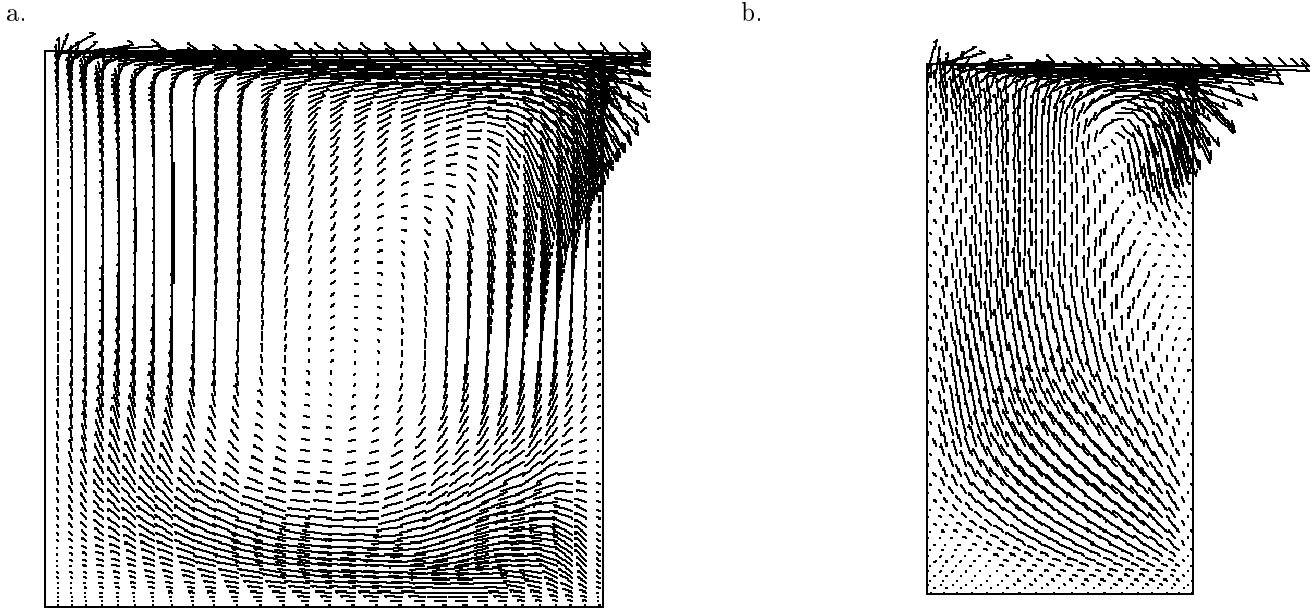


FIG. 4. Case A: primary flow in cross-sections with various aspect ratio: a) $CP2$ (aspect ratio 1 : 1) and b) $CP3$ (aspect ratio 0.5 : 1). The vector scale is doubled in comparison to that in Fig. 3.

upper front corner of the cavity in comparison to the 2-D flow in the cavity with the same aspect ratio.

The primary flow in planes $CP2$ and $CP3$ are presented in Fig. 4. In plane $CP2$, the vortex core slowly rotates at the cavity central part. The flow current is directed parallel to the side walls and along the cavity bottom. In plane $CP3$, the vortex center is shifted toward the upper right corner. The flow is directed upwards in the most of the section and does not contribute to the primary flow (which is parallel to the lid). Recall that the arrow scale is doubled in Fig. 4 in comparison to that in Fig. 3, i.e., the velocity in sections

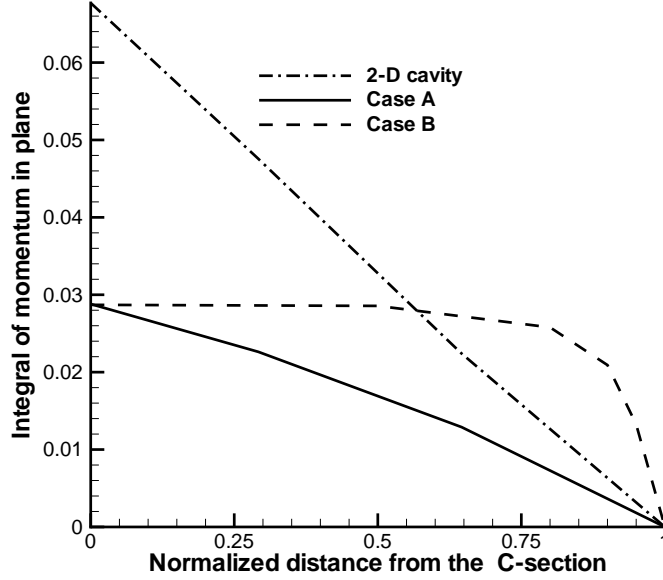


FIG. 5. The integral I_S of primary momentum

$CP2$ and $CP3$ is substantially smaller than that in the CP plane.

To make a quantitative comparison of the primary momentum transfer in Cases A and B, the volume and surface integrals of the flow momentum in the direction parallel to a moving lid are introduced. Since the lid direction in Case A is $(\vec{i} + \vec{k})/\sqrt{2}$, the expression for local momentum of primary velocity is given by $M_{\parallel} = 0.5(U + W)^2$. In Case B, the momentum of primary velocity is equal to $M_{\parallel} = W^2$. The volume integral of momentum is equal to

$$(1) \quad I_V = \frac{1}{V} \int_V M_{\parallel}.$$

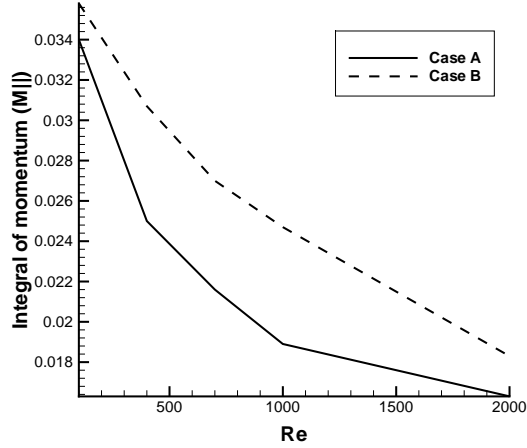
The surface integral is given by:

$$(2) \quad I_S = \frac{1}{S} \int_S M_{\parallel}.$$

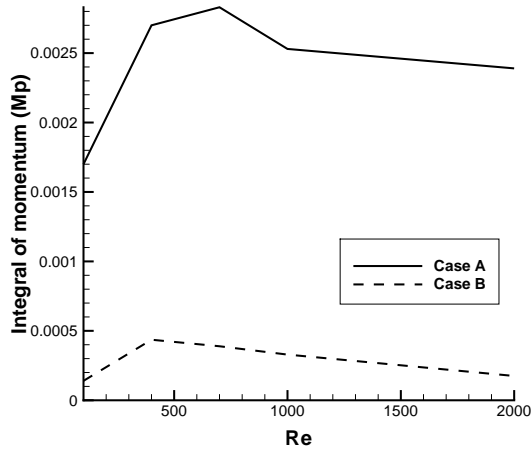
In Fig. 5, the integral I_S is plotted as a function of a normalized distance n measured from the section CP . In order to plot integrals (2) together for Cases A and B, the distance from the central plane is normalized by half-edge $1/2$ in Case B and half-diagonal $\sqrt{2}/2$ in Case A. In both cases, the I_S practically coincide at the central plane ($n = 0$). In Case B, the I_S remains constant for $n \leq 0.8$ and decreases toward the side wall for larger values of n . In other words, the “boundary layer” thickness is equal to 0.1 in Case B. In Case A, the I_S decreases gradually with n . The I_S and I_V are related by:

$$(3) \quad I_V = \int_{n=0}^{n=1} \phi(n) I_S(n) dn,$$

where the weight function $\phi(n) = 2(1 - n)$ in Case A and $\phi(n) = 1$ in Case B. In other words, the variable section area in Case A leads to a non-trivial weight function $\phi(n)$ and, therefore, the I_S of the mean



a.



b.

FIG. 6. Volume integral of momentum: a) I_V and b) I_\perp .

diagonal section CP in Case A has doubled weight in above formulae. For both cases, the volume integrals of momentum (1) are presented in Table 1 and in Fig. 6. Depending on the Re number, the integral of momentum is 20 – 30% larger in Case B than that in Case A.

The length of a 2-D CP section in Case A is

$$(4) \quad l = \sqrt{2}(1 - n).$$

For instance, $n = 0$ for CP ; $n = 1 - 1/\sqrt{2} \approx 0.292$ for $CP2$; and $n = 1 - 0.5/\sqrt{2} \approx 0.646$ for $CP3$. To compare the momentum transfer to that for 2-D cavities with the same aspect ratio, the computed I_S for 2-D cavities as a function of n is presented in Fig. 5. The 2-D cavity height is equal to unity while its length is computed by Eq. (4). In the 2-D case, the numerical method and the numerical grid used are the same as for 3-D cases (see the previous Section). The integral of momentum I_S for the 2-D $\sqrt{2} : 1$ cavity is 135% higher than that for the central section CP of Case A. The difference is 112% for $CP2$ and 29.9% for $CP3$. The difference is caused by the finite span in 3-D cavities and variable aspect ratio of longitudinal sections in Case A. For Case B, the finiteness of the cavity span leads to the 70% difference between I_S for CP section and the 2-D square cavity. Note that for the rectangular $1 : 1 : 3$ cavity of larger span (Section 5),

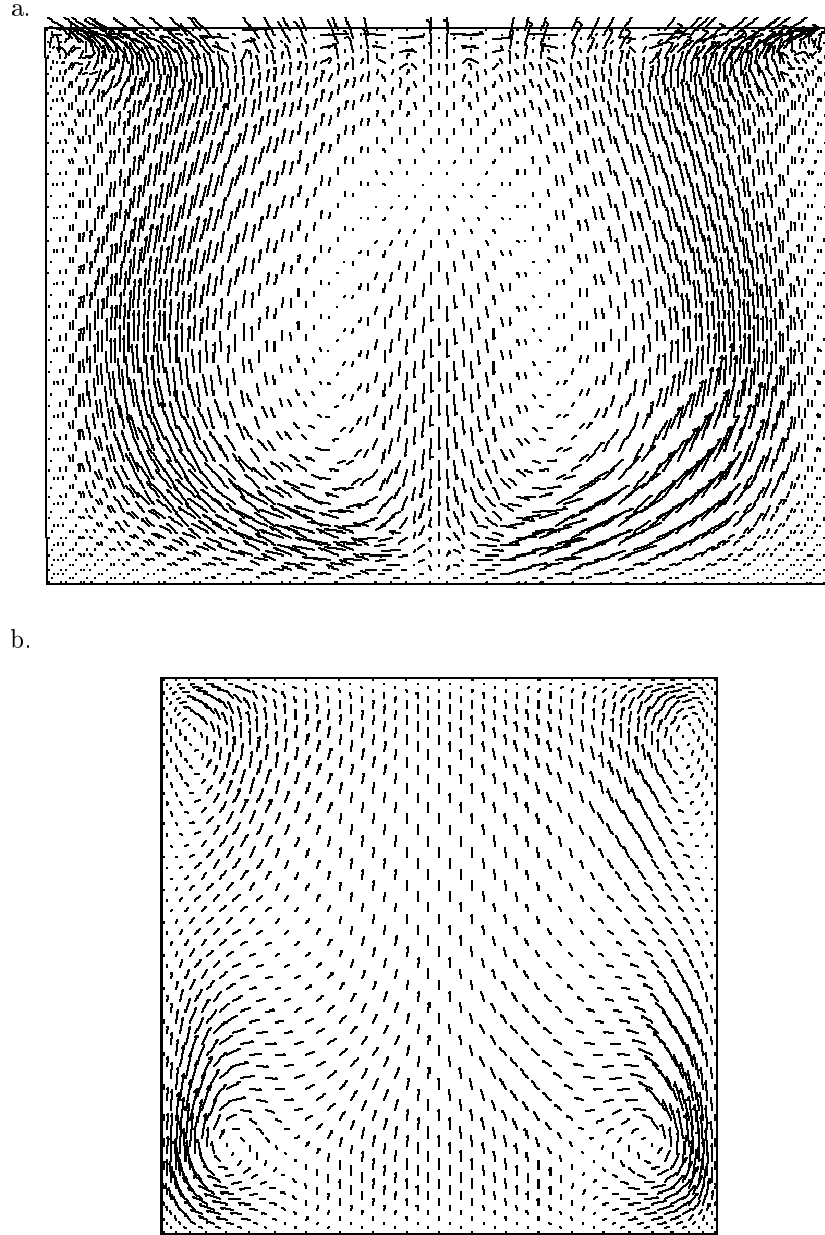


FIG. 7. Flow in the plane perpendicular to the direction of the lid ($Re = 700$): a) Case A; the vector scale is doubled in comparison to that in Fig. 3. b) Case B; the vector scale is four times larger than that in Fig. 3.

the difference in the cross-section reduces to 21.5%.

4. Secondary flow. The flow in the plane PP is shown in Figs. 7a,b for Cases A and B, respectively. In Case B, the vortices appear in the upper and lower corners of the section. In Case A, contrary to Case B, a vortex pair appears near the symmetry line. At the symmetry line there is a stagnation point located at $y = 0.74$. From the stagnation point, the flow is directed up towards the lid and down towards the cavity bottom. The vortex size and strength are considerably larger than those in Case B. (The vector scale is doubled in Fig. 7b in comparison to that in Fig. 7a)).

To make a quantitative comparison of transverse momentum transfer in Cases A and B, the momentum

TABLE 1
Volume integrals of momentum for 3-D cubical cavity

Re number	Case A		Case B	
	I_V	I_{\perp}	I_V	I_{\perp}
100	0.34E-01	0.17E-02	0.358E-01	0.14E-03
400	0.25E-01	0.27E-02	0.307E-01	0.436E-03
700	0.216E-01	0.283E-02	0.270E-01	0.389E-03
1000	0.189E-01	0.253E-02	0.247E-01	0.329E-03
2000	0.163E-01	0.239E-02	0.183E-01	0.175E-03

in the direction perpendicular to a moving lid were considered. Since the transverse direction in Case A is $(\vec{i} - \vec{k})/\sqrt{2}$, the expression for local transverse momentum is given by $M_{\perp} = 0.5(U - W)^2$. In Case B, the transverse momentum is equal to $M_{\perp} = U^2$. The volume-averaged value of integral of momentum is computed by

$$(5) \quad I_{\perp} = \frac{1}{V} \int_V M_{\perp}.$$

Integral I_{\perp} is about one order of magnitude larger in Case A than that in Case B (Fig. 6b). For $Re = 2000$, the I_{\perp} is of 14.66% of I_V in Case A whereas the I_{\perp} is of only 0.95% of I_V in Case B. In fact, much stronger transverse flow motion in Case A confirms this integral evaluation (compare Figs. 7a and 7b).

To study the transverse flow motion in the middle plane MP , the velocity vectors are shown in Figs. 8a-d and Figs. 9a-d for Cases A and B, respectively, and the range of Reynolds numbers within $100 < Re < 2000$. The plotted vector scale is the same in all Figs. 8-9 and equal to this in Fig. 7b. For $Re = 100$, the flow is parallel to the lid direction and no visible vortices are observed in Cases A and B. For $Re = 400$, the vortex couple appears in the MP corners in both Cases A and B and these vortices are designated as 1 in Fig. 8b. In Case B, the only vortex couple is visible for larger Re numbers (Figs. 9c,d). These vortices elongate towards the symmetry line with increase of the Reynolds number. As opposed to Case B, in Case A the number of vortex pairs increases with the Re number and five couples of vortices are visible and designated as 1, 2, 3, 4, and 5 in Fig. 8d ($Re = 2000$).

5. Rectangular cavity and turbulent flow. The computational results for a 3-D rectangular cavity with 1:1:3 depth-to-width-to-length ratio is considered. The cavity lid is 1:3 rectangle; the Re number is equal to 700. Three cases are modeled: (i) the lid moves along its diagonal (Case A); (ii) the lid moves along its long side (Case B1); and (iii) the lid moves along its short size (Case B2).

In Case B1, the strong vortices appear at the front corners where the flow impinges into the front wall of the cavity. The rest of computational volume includes weak vortices near side walls and strong back flow along the cavity axis. In Case B2, the vortices occupy the space near side walls up to the back wall. In Case B1, the volume-averaged integral I_V is larger and I_{\perp} is smaller than those in Case B2 (see Table 2). In Case A, the curvilinear stagnation line initially coincides with the diagonal of PM and then deviates towards the side wall. Non-symmetrical vortices with respect to the diagonal of the lid appear at both sides of the diagonal in the back part of the cavity. The value of integral of primary momentum I_V in Case A is between those for cases B1 and B2. On the contrary, the value of integral of secondary momentum I_{\perp} in Case A is approximately one order of magnitude larger than those in Cases B1 and B2.

TABLE 2
Volume integrals of momentum for rectangular cavity, $Re=700$

Case A		Case B1		Case B2	
I_V	I_{\perp}	I_V	I_{\perp}	I_V	I_{\perp}
0.403E-01	0.324E-02	0.460E-01	0.217E-03	0.359E-01	0.411E-03

The goal of this study is to investigate the cavity flow for Re numbers corresponding to existence of steady solution for such a flow. Nevertheless, the Görtler numbers for Cases A and B based on steady flowfield are computed to indicate that the transition to unsteady flow may occur for smaller Re numbers in Case A.

The profile of vertical velocity V along the middle line ML is shown in Fig. 12 for Cases A and B for $Re = 700$. In Case A, the abscissa has been scaled by $\sqrt{2}$. The absolute value of maximum velocity is 0.65 in Case A and 0.43 in the Case B. Along the line RL , the ratio of the maximum absolute velocities is approximately equal to 1.5 as well. The thickness of boundary layer estimated by the distance from the wall to the point of maximum velocity is the same in Cases A and B. However, the actual thickness of the boundary layer in Case A is $\sqrt{2}$ larger because of scaling. The Görtler number is based on the boundary layer Reynolds number, the boundary layer thickness and the radius of curvature of the wall [10]:

$$(6) \quad G = \frac{Re^2 \delta}{r_c},$$

where $Re = U_{max} \delta / \nu$ is the boundary layer Reynolds number, δ is the boundary layer thickness, and r_c is the radius of curvature of the wall. Authors[10] assume that r_c is equal to the half-length of cross-section, i.e., $r_c = 1/2$ in Case B and $r_c = \sqrt{2}/2$ in Case A. The ratio of Görtler numbers in Cases A and B is given by: $G_A/G_B = 1.5^2 \sqrt{2}^3 / \sqrt{2} = 4.5$. Therefore, the unsteady Görtler vortices may appear at smaller Re numbers in comparison with Case B and may convect to the peripheral parts of the cavity by transverse flow.

For the turbulent flow in cubical cavity the Navier-Stokes equations are replaced with the Reynolds-averaged steady equations and the Reynolds stress model of turbulence [15]. The Launder and Spalding [16] wall functions are used for boundary conditions for the Reynolds stresses.

For $Re > 2000$, the cavity flow becomes unsteady. Previous experimental [18] and computational [23] studies of Case B for $3000 \leq Re \leq 10000$ show that the cavity flow is unsteady with high- (turbulent) and low-frequency (organized structure) fluctuations of velocity around time-averaged values. While for $Re \approx 3000$ the fluctuations are due to low-frequency meandering of Görtler vortices, the break-down of organized Görtler vortices is observed for $Re = 10000$ and the high-frequency turbulent fluctuations become responsible for momentum transfer. This type of unsteadiness is modeled using the RANS approach in the current study. Still, the presence of single vortices sweeping through the computational volume is quite possible and may affect the momentum transfer [18]. An assumption about the presence of steady solution to RANS equations is adopted in this study and the effect of low-frequency unsteady vortex shedding will be considered in our future research.

The flowfield in the cross-section CP is shown in Fig. 13 for $Re = 40000$. For $Re = 10000$, the flowfield shows similar vortical pattern. To compare with the laminar flowfield in Case A, each of two central vortices is split into three unequal vortices (compare Figs. 7a and 13a). The corner flow separation leads to formation of vortices in four corners of section CP , which are not visible in the laminar case. In Case B, the corner vortices are split and the vortical area is shifted toward the vertical centerline (compare Figs. 7b and 13b). For Case A, five pairs of vortices are observed. Their location in the mid-section MP is similar to that for

TABLE 3
Volume integrals of momentum for turbulent cubical cavity flow

Re	Case A		Case B	
	I_V	I_{\perp}	I_V	I_{\perp}
10000	0.717E-02	0.120E-02	0.967E-02	0.162E-03
40000	0.365E-02	0.681E-03	0.414E-02	0.540E-04

laminar flow ($Re = 2000$) and turbulent flow (compare Figs. 8d with 14a). In Case A and $Re = 40000$, the integral of momentum of transverse motion makes 18.6% of the integral of primary momentum (see Table 3). For Case B, the flowfield pattern is quite different for turbulent and laminar flows (compare Figs. 9 and 14b). Numerous vortices appear at the front and back parts of the section MP . Nevertheless, there is no significant increase of transversal part of momentum as a fraction of primary momentum since the integral of momentum of transverse motion I_{\perp} is of 1.3% of the integral of primary momentum I_V . For $Re = 10000$, the ratio between different components of flow momentum remains approximately the same (see Table 3) while the values of I_V and I_{\perp} are doubled in comparison to those for $Re = 40000$.

6. Conclusion and future plans. The cavity flow driven by the cavity lid moving along its diagonal is simulated using the the second-order upwind discretizations of convection terms. This flow mimics environmental and aeronautical flows where the governing flow direction is not parallel to cavity side walls. The considered flow (Case A) is substantially different from that in the benchmark case where the cavity lid moves parallel to the side walls of the cavity (Case B). Enhanced transverse fluid motion in the direction perpendicular to the direction of moving lid is observed in Case A. The integral of momentum in this direction is about one order of magnitude higher than that in Case B. The number and location of vortices in the mid-plane (MP the lid) is quite different from that in Case B, where only corner vortices appear. In Case A, the number of vortices increases with the Re number and these vortices appear at the central part of the mid-plane.

The flow in the 3-D elongated cavity driven by the cavity lid has the curvilinear separation line and non-symmetric vortices in the mid-plane. Again, the integral of transverse momentum is approximately one order of magnitude higher than those in benchmark cases B, where the lid moves parallel to either long or short side walls.

For diagonal-driven fully developed turbulent cavity flow in a cube, modeled by the Reynolds Stress model of turbulence, the vortical pattern is qualitatively similar to that for the laminar flow at $Re = 2000$. For Case B, significantly more secondary vortices are observed in planes PP and MPa than for laminar flow case. Nevertheless, the transverse momentum for Case A remains more than one order of magnitude higher than that for Case B, i.e., the strong yaw-related amplification of transversed flow holds for turbulent Re numbers.

For the main diagonal plane in Case A, the Görtler number appears to be 4.5 times larger than that for Case B for the same Re number. Therefore, the unsteady Görtler vortices may appear at smaller Re numbers than in Case B. Although the second-order discretizations is accurate enough for the viscous and steady flow, higher order numerical schemes are required for wavy and unsteady transition phenomena. The high-order numerical modeling of transition to unsteady flow including Görtler vortices will be conducted in our future research.

REFERENCES

- [1] *FLUENT 5.0 User's Manual*, Fluent Inc., Lebanon, NH, 2000. <http://www.fluent.com>.
- [2] C. K. AIDUN, N. G. TRIANTAFILLOPOULOS, AND J. D. BENSON, *Global Stability of a Lid-driven Cavity with Throughflow: Flow Visualization Studies*, *Physics of Fluids A*, 3 (1991), pp. 2081–2091.
- [3] V. BABU AND S. KORPELA, *Numerical Solution of the Incompressible Three-dimensional Navier-Stokes Equations*, *Computers and Fluids*, 23 (1994), pp. 675–691.
- [4] T. J. BARTH AND D. JESPERSEN, *The design and application of upwind schemes on unstructured meshes*, in *Proceedings of the 6th AIAA 27th Aerospace Sciences Meeting*, Reno, Nevada, 1989. AIAA Paper 89-0366.
- [5] T. CHIANG, W. SHEU, AND R. HWANG, *Effect of Reynolds Number on the Eddy Structure in a Lid-driven Cavity*, *Int. J. for Numerical Methods in Fluids*, 26 (1998), pp. 557–579.
- [6] D. G. CRIGHTON, *Airframe noise*, in *Aeroacoustics of Flight Vehicles: Theory and Practice. Volume 1: Noise Sources*, H. H. Hubbard, ed., New York, 1991, pp. 391–447. NASA Reference Publication 1258, WRDC Technical Report 90-3052.
- [7] M. CZECH, E. SAVORY, N. TOY, AND T. MAVRIDES, *Aeroacoustic phenomena associated with yawed rectangular cavities*, in *Proceedings of the 21st Aeroacoustics Conference*, Lahaina, HI, 2000. AIAA Paper 2000-1901.
- [8] P. J. DISIMILE, N. TOY, AND E. SAVORY, *Pressure Oscillations in a Subsonic Cavity at Yaw*, *AIAA Journal*, 36 (1998), pp. 1141–1148.
- [9] W. DOBRZYNSKI, L. CHOW, P. GUION, AND D. SHIELLS, *A European Study on Landing Gear Airframe Noise Sources Cavities*, in *Proceedings of the 21st Aeroacoustics Conference*, Lahaina, HI, 2000. AIAA Paper 2000-1971.
- [10] C. J. FREITAS AND R. STREET, *Non-linear Transient Phenomena in a Complex Recirculating Flow: A Numerical Investigation*, *Int. J. for Numerical Methods in Fluids*, 8 (1988), pp. 769–802.
- [11] C. HIRSCH, *Numerical Computation of Internal and External Flows, Vol. 1: Fundamentals of Numerical Discretizations*, John Wiley, New York, 1994.
- [12] R. IWATSU, K. ISHII, T. KAWAMURA, K. KUWAHARA, AND J. HYUN, *Numerical Simulation of Three-dimensional Flow Structure in a Driven Cavity*, *Fluid Dynamics Research*, 5 (1989), pp. 173–189.
- [13] J. R. KOSEFF AND R. L. STREET, *Visualization Studies of a Shear Driven Three-dimensional Recirculating Flow*, *J. Fluid Eng.*, 106 (1984), pp. 21–29.
- [14] H. KU, R. HIRSH, AND T. TAYLOR, *A Pseudospectral Method for Solution of the Three-dimensional Incompressible Navier-Stokes Equations*, *J. Comput. Phys.*, 70 (1987), pp. 439–462.
- [15] B. LAUNDER, G. REECE, AND W. RODI, *Progress in the Development of a Reynolds-Stress Turbulence Closure*, *Journal of Fluid Mechanics*, 68 (1975), pp. 537–566.
- [16] B. LAUNDER AND D. SPALDING, *The Numerical Computation of Turbulent Flows*, *Computer Methods in Applied Mechanics and Engineering*, 3 (1974), pp. 269–289.
- [17] S. PATANKAR, *Numerical Heat Transfer and Fluid Flow*, Hemisphere Publishing Co., New York, 1980.
- [18] A. K. PRASAD AND J. R. KOSEFF, *Reynolds number and end-wall effects on a lid-driven cavity flow*, *Physics of Fluids A*, 1 (1989), pp. 208–219.
- [19] C. M. TEIXEIRA, *Digital Physics Simulation of Lid-driven Cavity Flow*, *International Journal of Modern Physics C*, 8 (1997), pp. 685–696.
- [20] M. ULF AND W. QIAO, *Directivity of landing-gear noise based on flyover measurements*, in 5th

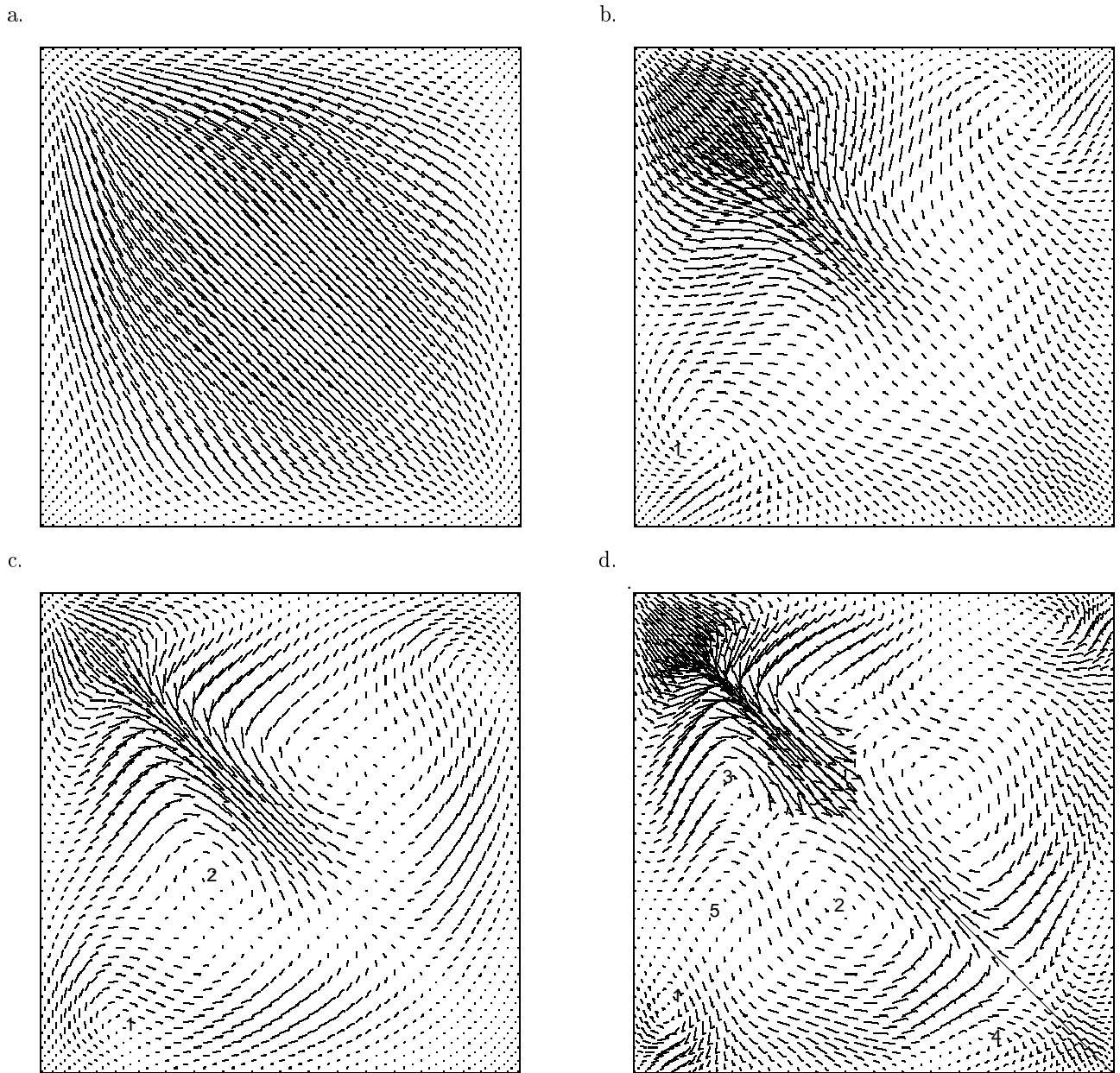
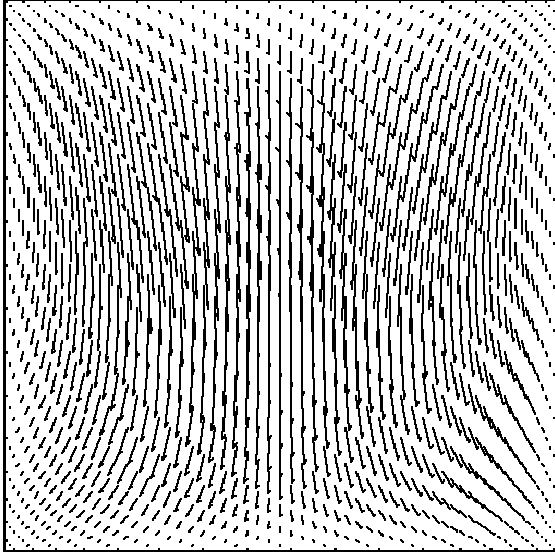


FIG. 8. Flow in 3-D cubical cavity in Case A: a) $Re = 100$, b) $Re = 400$, c) $Re = 700$, and d) $Re = 2000$.

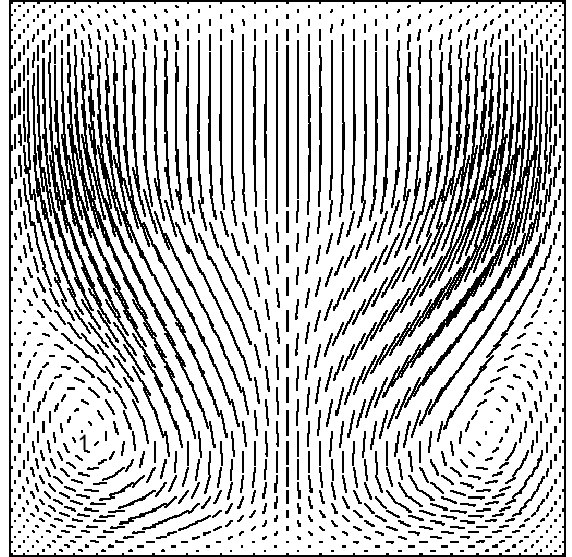
AIAA/CEAS Aeroacoustics Conference, Bellevue, WA, 1999. AIAA Paper 99-1956.

- [21] J. P. VANDOORMAAL AND G. D. RAITHY, *Enhancements of the SIMPLE Method for Predicting Incompressible Fluid Flows*, Numer. Heat Transfer, 7 (1984), pp. 147–163.
- [22] M. WANG AND T. SHEU, *An Element-by-element BICGSTAB iterative method for three-dimensional steady Navier-Stokes equations*, J. of Computational and Applied Mathematics, 79 (1997), pp. 147–165.
- [23] Y. ZANG, R. L. STREET, AND J. R. KOSEFF, *A Dynamic Mixed Subgrid-scale Model and Its Application to Turbulent Recirculating Flows*, Physics of Fluids A, 5 (1993), pp. 3186–3196.

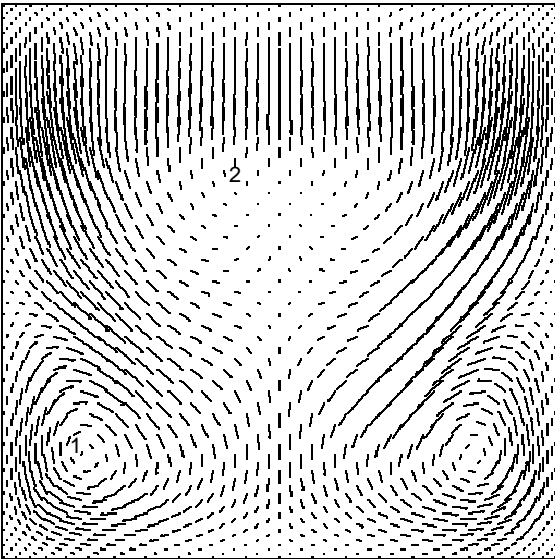
a.



b.



c.



d.

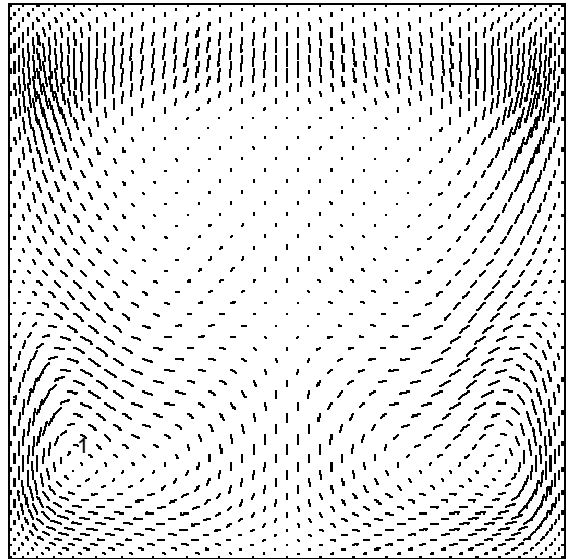


FIG. 9. Flow in 3-D cubical cavity in Case B: a) $Re = 100$, b) $Re = 400$, c) $Re = 700$, and d) $Re = 2000$.

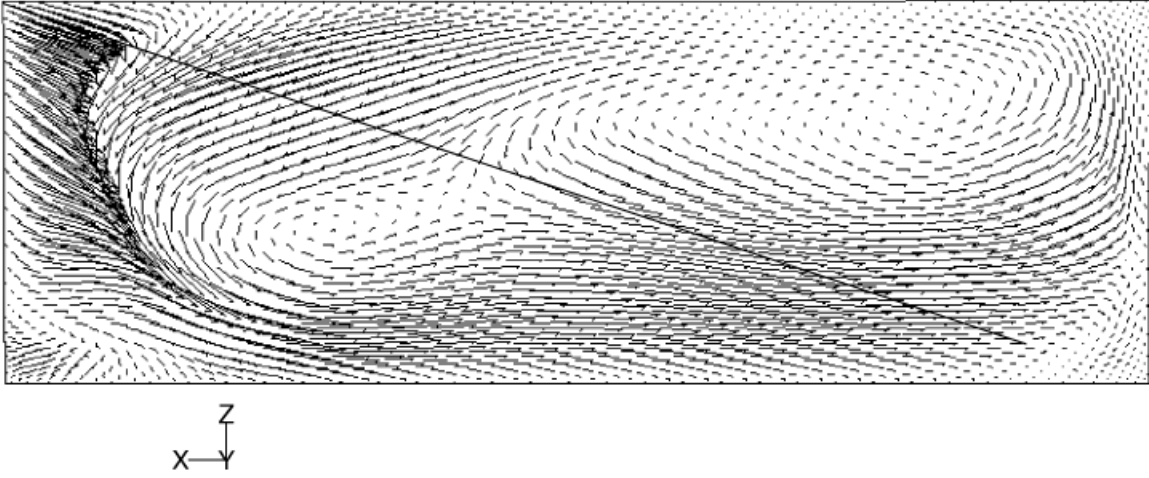
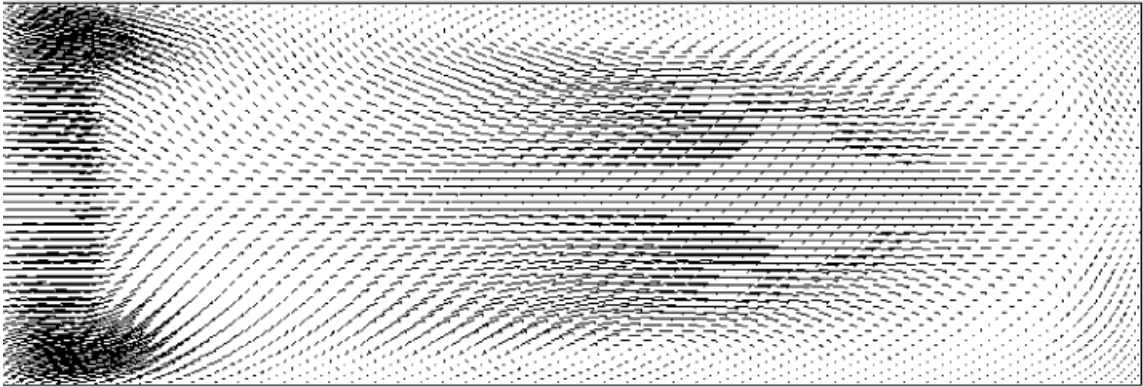


FIG. 10. *Flow in rectangular cavity in Case A.*

a.



b.

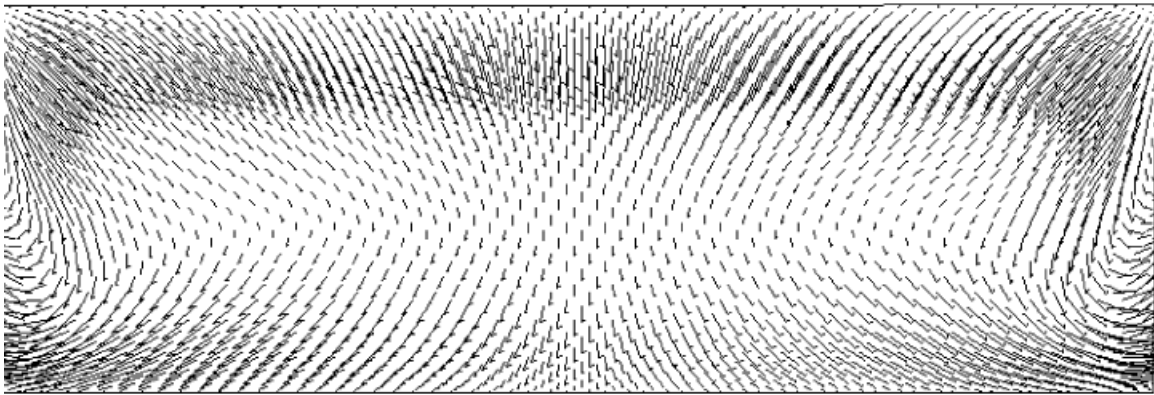


FIG. 11. *Flow in rectangular cavity: a) the lid moves along long side (Case B1) and b) the lid moves along short side (Case B2).*

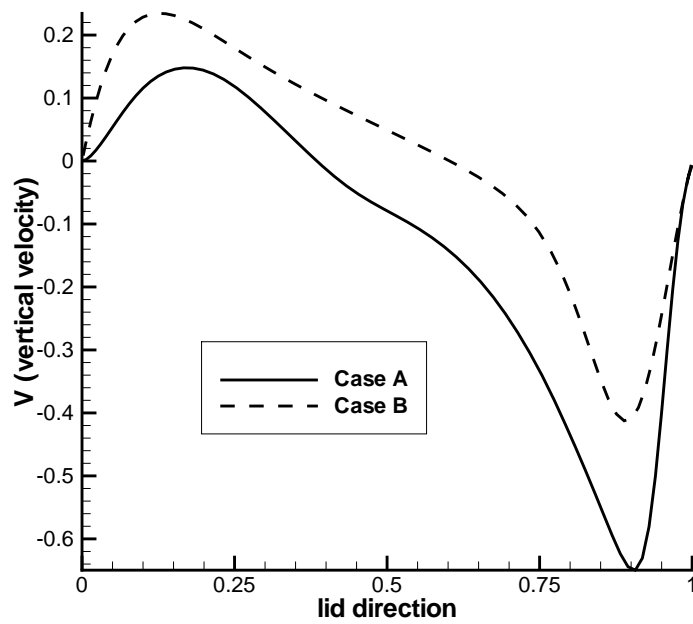


FIG. 12. *Velocity profile along the line ML.*

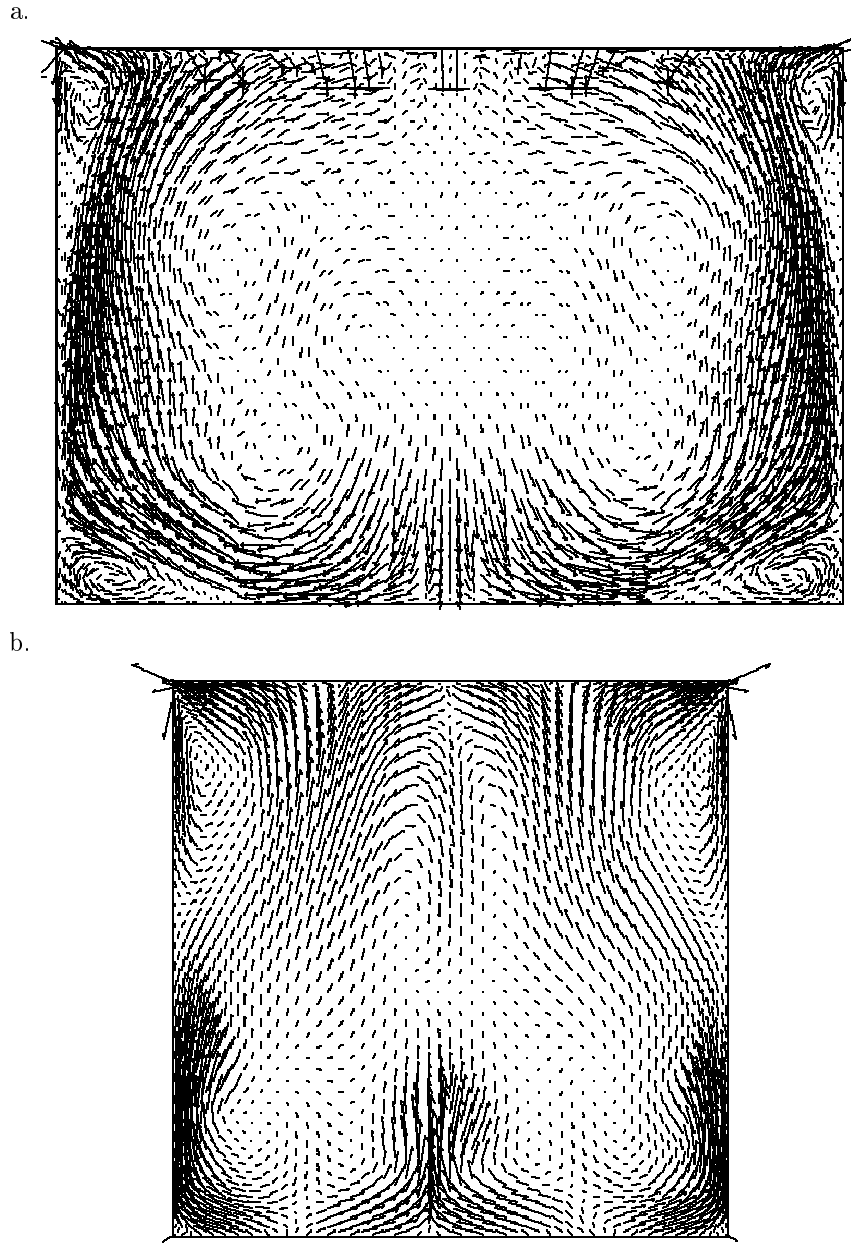


FIG. 13. *Turbulent cavity flow in the plane perpendicular to the direction of the lid. a) Case A: the vector scale is six times larger than that in Fig. 3; b) Case B: The vector scale is twelve times larger than that in Fig. 3.*

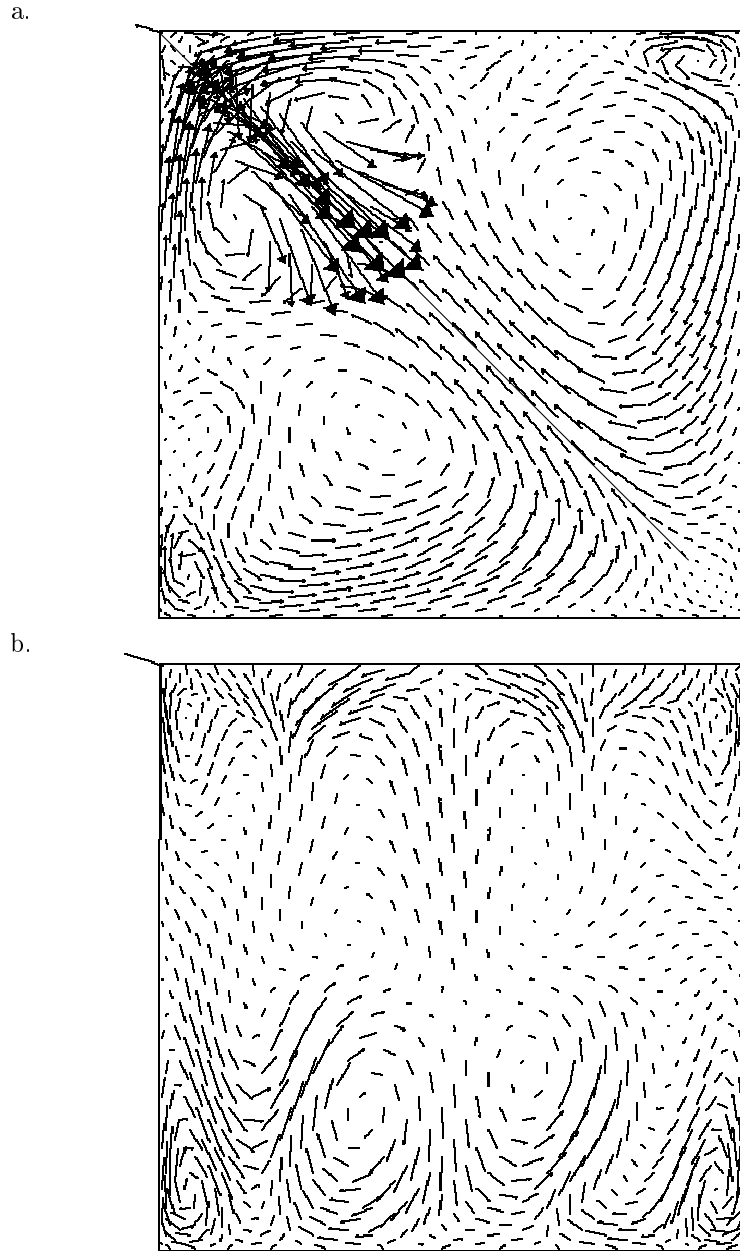


FIG. 14. *Turbulent cavity flow in the middle plane MP: a) Case A; b) Case B. The vector scale is twelve times larger than that in Fig. 3.*